# Design, Fabrication, and Testing of a Monolithic Biaxial Architecture for MEMS Accelerometers

**TR-CIM-2019-15-10-01**

Xiaowei Shan, Jorge Angeles and

James Richard Forbes


*Centre for Intelligent Machines, Department of Mechanical Engineering*
McGill University, Montréal, Canada

# Design, Fabrication, and Testing of a Monolithic Biaxial Architecture for MEMS Accelerometers

**Xiaowei Shan***
PhD graduate, Student Member of ASME
Department of Mechanical Engineering
McGill University
Montreal, Quebec, Canada, H3A 0G4
Email: xiaowei.shan@mail.mcgill.ca

**Jorge Angeles**
Professor, Fellow of ASME
Department of Mechanical Engineering
McGill University
Montreal, Quebec, Canada, H3A 0G4
Email: angeles@cim.mcgill.ca

**James Richard Forbes**
Assistant Professor
Department of Mechanical Engineering
McGill University
Montreal, Quebec, Canada, H3A 0G4
Email: james.richard.forbes@mcgill.ca

*A monolithic biaxial architecture is designed, fabricated and tested for MEMS accelerometers with isotropic stiffness in the sensitive plane and high frequency ratios between the insensitive and sensitive directions. The architecture is designed to accommodate any regular polygonal shape with a proof-mass suspension made of a serial array of parallelogram linkages. Structural optimization is conducted for high frequency ratios and a high degree of compliance in the suspension, for low-g applications and planar actuation. Vibration tests are conducted in the MEMS prototypes and validate the isotropic sensitivity of the biaxial architecture.*

## 1 Introduction

This paper focuses on the development of a biaxial architecture, dubbed "Orchid", with high in-plane and low off-plane sensitivity. The Orchid architecture under study is only sensitive to translational accelerations in the sensitive plane, and insensitive to both the out-of-plane translational and rotational motions in the in- and out-of-plane directions. The choice of the biaxial sensitivity is mainly considered for the estimation of not only the rigid-body acceleration, but also the velocity field and the body pose with a strapdown [1].

Within the design of biaxial MEMS accelerometers, off-plane insensitivity and isotropic sensitivity are emphasized in terms of instrument frequency response. Various proof-mass suspensions have been proposed for biaxial accelerometers [2–6], mostly with resonant or capacitive sensing. Particularly, what we have termed Simplicial-Biaxial-Accelerometers (SBAs) [7, 8] use a serial array of two parallelogram four-bar linkages—such a linkage is called a "Π-joint" within the mechanisms literature [9], the array termed a ΠΠ-joint, or ΠΠ-hinge, to provide in-plane stiffness isotropy, which lies at the foundations of the Orchid architecture design.

In the Orchid architecture design, the requirement of the compliant mechanism design attached to large masses is beneficial for low-$g$ applications, but is challenged by that of mechanical robustness [10–12]. To resolve the conflict between the fragility of the compliant suspension and the large proof-mass, the Orchid structures are optimized with regard to both the frequency ratio and stress concentration. Because of the scale feature of the Orchid prototypes, techniques are also integrated for the vibration test setup to detect micro-scale motions with moderate acceleration, yet enough excitation.

The novel contributions of this paper are a class of biaxial architecture design that can yield high frequency ratios between the nonsensitive and sensitive directions and the techniques for fabricating and testing MEMS structures between micro and macro dimensions.

## 2 Design and Optimization of the Orchid Architecture

### 2.1 Architecture Design and Parameterization

The *Orchid architecture* is illustrated in Fig. 1(a), whose parts are named after the orchid corresponding parts, as per Fig. 1(b). The coordinate frames and structural parameters are defined in Fig. 1(a). Let: $\{O, \mathcal{X}, \mathcal{Y}, \mathcal{Z}\}$ be the reference frame $\mathcal{F}$, with its origin $O$ located at the centroid of the equilateral triangle; its $\mathcal{Y}$-axis be one of the axes of symmetry of the equilateral triangle; and its $\mathcal{Z}$-axis be normal to the wafer surface, its $\mathcal{X}$-axis following the right-hand rule.

*Address all correspondence related to ASME style format and figures to this author.

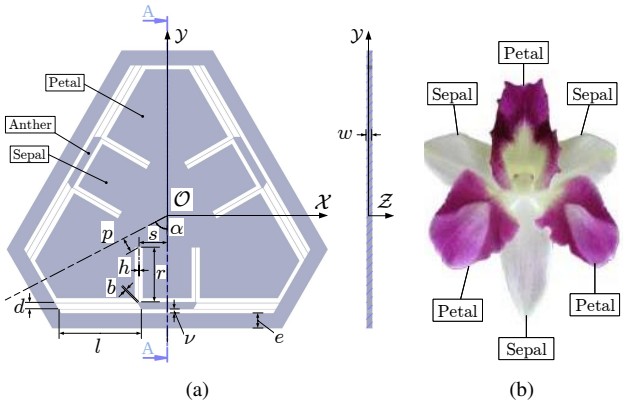


(a) (b)

Fig. 1. Orchid architecture: (a) parameters; (b) an orchid flower[1]

Since the architecture is axially and periodically symmetric, only an $\alpha/2\pi$ portion of the structure need be parametrized, as per the labels in Fig. 1(a). The pertinent parameters are listed below: $s$, half the width of the "sepal"; $p$, half the width of the "petal"; $h$, the width of the "hinge" that stretches out as a "filament"; $r$, the length of the "radial" hinge; $b$, the length of the 45°-line on the "bar"-shaped "anther"; $l$, the length of the "lateral" hinge; $d$, the "distance" between the lateral hinges; $v$, the gap width (borrowing "v" from French "vide", for "gap", as "g" is reserved for the gravity acceleration) between the proof-mass, the frame and the hinges pairwise; $e$, the width of the frame "edge"; $w$, the thickness of the "wafer"; $\alpha$, the angle describing the regular polygonal shape of the accelerometer.

Moreover, the architecture can be based on any regular polygonal shape, in which the triangular (Orchid) and square (four-petal-Orchid) shapes allow for the lowest in-plane stiffness, thereby meeting specifications of low fundamental frequencies for navigation applications [10].

### 2.2 Dimensional and Frequency Optimization

For convenience of testing the mechanical properties, the structure is designed with relatively large dimensions within the micro scale. A wafer thickness of $w = 500$ $\mu$m is adopted for a high aspect ratio of the hinges, aiming at a high frequency ratio of the structure. The key parameters for the proof-mass suspension are $r$, $b$, $d$, $l$ and $s$; hence, the design parameters are set to be the first four, leaving $s = p = 1000$ $\mu$m to avoid narrow connection of the "petals" and "sepals" to the center area. As thin hinges put the structure at the risk of fracture, we chose $h = 30$ $\mu$m, with an aspect ratio of 16.7 for the 500-$\mu$m wafer. The width of the gaps $v$ will then be determined by the mobility range of the optimum structure under a prescribed acceleration range.

The dimensional optimization was conducted using the goal-driven optimization in ANSYS Workbench with the *response-surface* method. Two goals are set: one is to maximize the lowest frequency ratio between the insensitive and sensitive axes. The other is to screen out the samples with the difference of the first two natural frequencies smaller than 30 Hz, which eliminates the samples whose first mode is not the in-plane translation.

Within the structural optimization, the frequency ratios between the insensitive and sensitive motions increase, while the frequency difference among the insensitive motions decreases. Finally the frequencies reach a balance, with the optimum key dimensions of $l = 3314.3$, $r = 2301.2$, $b = 142.75$, $d = 465.68$ and $v = 150$. The overall size is 14.28 mm when $e = 800$ $\mu$m for an arbitrary width of the frame. A finite-element (FE) modal analysis is then conducted for the optimum structure, denoted "W500P3"[2]; the natural frequencies and frequency ratios are listed in Table 1. The first six mode shapes are illustrated in Fig. 2.

Table 1. Natural frequencies of Orchid W500P3

| $i$ | 1 | 2 | 3 | 4 | 5 | 6 |
|---|---|---|---|---|---|---|
| $f_i$ (Hz) | 545.9 | 546.4 | 3470.1 | 3478.3 | 4729.9 | 4730.3 |
| $f_i/f_1$ | 1.0 | 1.0008 | 6.3564 | 6.3716 | 8.6641 | 8.6649 |

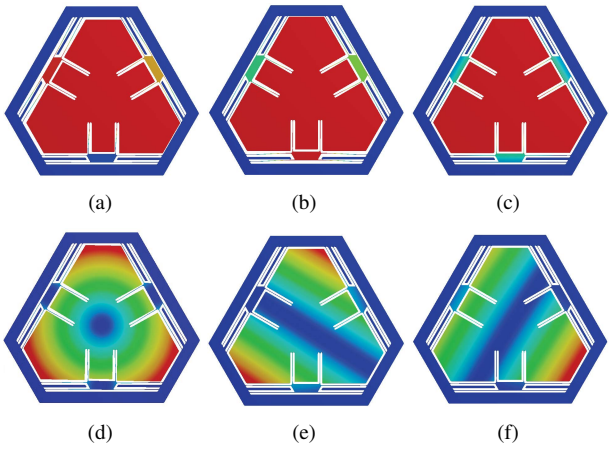

(a) (b) (c) (d) (e) (f)

Fig. 2. Mode shapes[4] of W500P3: (a) mode 1 ($t_x$); (b) mode 2 ($t_y$); (c) mode 3 ($t_z$); (d) mode 4 ($r_z$); (e) mode 5 ($r_y$); (f) mode 6 ($r_x$)

Figures 2(a)–(c) pertain to translations in the directions of the $\mathcal{X}$-, $\mathcal{Y}$- and $\mathcal{Z}$-axes, respectively. At higher frequencies, rotations appear, as shown in Figs. 2(d)–(f). The Orchid W500P3 has a frequency ratio of 6.36 under an aspect ratio of 16.7. The in-plane frequency is around 546 Hz, that is, within the hecto-Hertz bandwidth for low-$g$ applications. This biaxial structure is only sensitive to translational accelerations in the sensitive plane, and insensitive to both the out-of-plane translation and rotational motions.

[1] Reproduced from `http://www.repotme.com/orchid-care/Orchid-Blooming.html/`

[2] "WxPy": the letters x and y indicate the wafer thickness and the polygonal shape of the structure

[4] $t_i$ $(i = x, y, z)$ denotes translation along the $i$th-axis; $r_i$ $(i = z, y, x)$ denotes rotation around the out-of-plane axis and two orthogonal in-plane axes.

Based on the lowest frequency ratio of W500P3 in Table 1, the ratio between the frequency ratio to the aspect ratio, or the frequency-to-aspect ratio for short, is calculated to be 0.381. Table 2 lists the key frequencies, the aspect ratios and the frequency-to-aspect ratio of three biaxial accelerometer designs in the literature, compared with Orchid W500P3. It can be seen that the Orchid structure is superior in terms of frequency ratio and the frequency-to-aspect ratio.

Table 2. Comparison of monolithic biaxial accelerometers

| Design | Orchid W500P3 | [8] | [5] | [4] |
|---|---|---|---|---|
| SF (Hz) | 545.9 | 5858.3 | 3699 | 1640 |
| LIF (Hz) | 3470.1 | 12890 | 3866 | 2500 |
| Frequency ratio | 6.36 | 2.20 | 1.05 | 1.55 |
| Aspect ratio | 16.7 | 15 | 8.75 | 11.54 |
| FTA ratio | 0.381 | 0.147 | 0.119 | 0.13 |

Note: sensitive frequency (SF), lowest insensitive frequency (LIF), frequency-to-aspect (FTA)

### 2.3 Stress Mitigation

To improve the stress distribution and to avoid failure during operation, the Orchid W500P3 is filleted with Lamé curves, which provide $G^2$-continuity at the fillet blending points. The $n$-order Lamé curve takes the simple form [13]

$$f(x,y) = x^n + y^n - 1 = 0. \tag{1}$$

in which $x$ and $y$ are assumed to be dimensionless.

For the fourth-degree Lamé curve with origin $(x_0, y_0)$ in the reference frame and intercepts $\boldsymbol{r}_a = [r_a, 0]^T$, $\boldsymbol{r}_b = [0, r_b]^T$ in the local frame, Eq. (1) is rewritten as

$$\left(\frac{x_l + x_0}{r_a}\right)^4 + \left(\frac{y_l + y_0}{r_b}\right)^4 = 1, \tag{2}$$

where $(x_l, y_l)$ in the reference frame denotes the in-plane coordinates of a point on the Lamé curve.

The fourth-degree Lamé curve is developed in Solidworks with equation-driven curves; hence, the parametric expressions of $x_l$ and $y_l$ in terms of angle $\phi \in [0, 2\pi]$ are derived from Eq. (2):

$$\begin{aligned} x_l &= r_a \frac{\cos\phi}{\left(\cos^4\phi + \sin^4\phi\right)^{1/4}} - x_0, \\ y_l &= r_b \frac{\sin\phi}{\left(\cos^4\phi + \sin^4\phi\right)^{1/4}} - y_0. \end{aligned} \tag{3}$$

For the corners and edges at angles other than $\pi/2$, the expressions of the Lamé curves are derived from the most general affine transformation in 2D, whose transformation matrix takes the form

$$\boldsymbol{T} = \boldsymbol{P}'\boldsymbol{P}^{-1}, \quad \boldsymbol{P} = [\boldsymbol{r}_a \;\; \boldsymbol{r}_b], \quad \boldsymbol{P}' = [\boldsymbol{r}_a \;\; \boldsymbol{Q}\boldsymbol{r}_b], \tag{4}$$

and $\boldsymbol{Q}$ is the 2D-rotation matrix through the angle given by the corner or edge.

An acceleration of 10 $g$ per axis is applied on W500P3 to simulate the static response. The distribution of the von Mises stress and the Lamé-filleted corner between the proof-mass and the hinge are shown in Fig. 3.

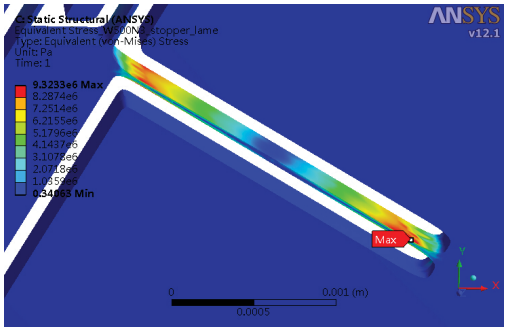


Fig. 3. Von Mises stress distribution of the Lamé-filleted W500P3

The maximum von Mises stress in the filleted Orchid structures occur at the radial hinge, instead of the corners formed by the hinges and the proof-mass. The maximum stress of 9.3233 MPa is three orders of magnitude below the yield strength of silicon, which is 7 GPa.

## 3 Prototyping and Vibration Tests

### 3.1 Microfabrication

The Orchid accelerometer prototypes were fabricated at both McGill Nanotools Microfab[5] and LMF of École Polytechnique de Montréal[6] to test the feasibility of microfabrication. The successful triangular W500P3-lame and square W500P4-circ are examined under microscope. Figure 4 reveals the difference of Lamé-curve and circular fillets for triangular and square Orchid structures, respectively. The white bar at the bottom-right corners is a 500 $\mu$m scale.

The prototypes were then tested with a laser-sensing system. To solve the reflectivity problem of the prototype surface with the laser beam, two methods are proposed: reflective tape on the c.o.m. of the proof-mass and spray powder for uniform coverage of the prototype surface. The texture of the reflective tape under microscopic view is shown in

[5]McGill Nanotools Microfab, McGill Institute for Advanced Materials, Ernest Rutherford Building, 3600 University St. Montreal, Quebec, H3A 2T8, Canada.

[6]Laboratoire de Microfabrication (LMF), Département de Génie Physique, Pavillon J.A.B., Campus de l'Université de Montréal, 2500 chemin de Polytechnique, Montréal, Québec, H3T 1J4, Canada

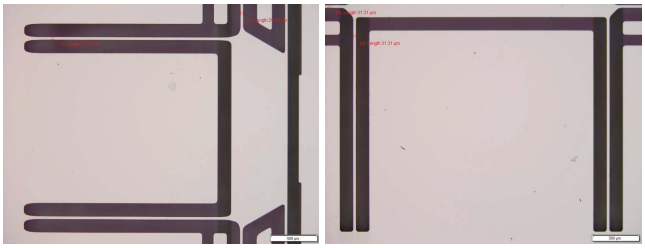

(a) (b)

Fig. 4. Hinge suspensions of W500P3-lame and W500P4-circ under the microscope: (a) W500P3-lame; (b) W500P4-circ

Fig. 5(a). It can be observed that the reflective tape has enormous shiny granules for scatter reflection. The texture comparison of the reflective tape and the spray powder on the channeled prototypes is shown in Fig. 5(b).

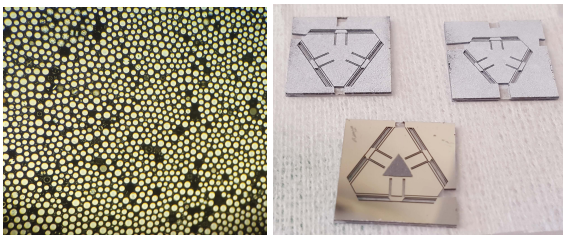

(a) (b)

Fig. 5. Texture of the reflective tape and spray powder: (a) microscopic view of the tape; (b) comparison of reflectivity

The spray powder solution was inspired by 3D-scanning techniques[7], where talcum powder is sprayed onto the target surface to change the reflectivity from directed, as a mirror, to scattered, as an opaque body. Instead of using special powder generally in large quantities and with long leading time, some grocery powder sprays work satisfactorily[8], since they come out liquid, dry fast and stay firmly on the target.

A potential problem of the reflective tape is the mass unbalance caused by the misalignment error, while the extra mass added by the powder is more uniformly distributed on the proof-mass. Under the microscope, the powder may hide a broken hinge and bring about difficulties for examination of the prototype integrity.

### 3.2 Test setup and results

To validate the mechanical properties of the proposed Orchid biaxial architecture, vibration tests were conducted on the WxPy prototypes for the in-plane and out-of-plane frequencies. The test setup is shown in Fig. 6. Generally speaking, the relative motion of the accelerometer sample to the mini shaker is detected by the fiber optic vibrometer, then recorded and interpreted by the micro system analyzer.

[7]http://www.3dreveng.com/2014/12/3d-scanning-tips/

[8]such as Dr. Scholl's Odour Destroyers Sneaker Treater.

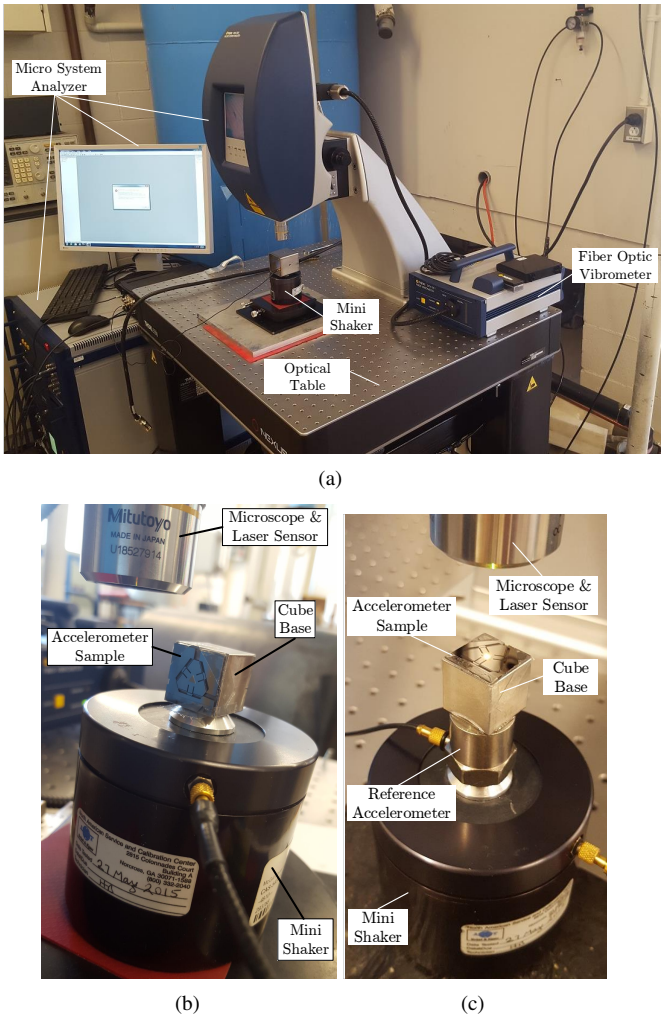


(a)

(b) (c)

Fig. 6. Vibration tests: (a) equipments; (b) setup for in-plane vibration; (c) setup for out-of-plane vibration

In Fig. 6(b), the accelerometer sample was pasted in three positions on a steel cube that was bonded to the shaker shaft. Each position has one axis of interest aligned with the shaking axis. Hence, four vibration tests are needed for the two in-plane and one out-of-plane translations, as well as for the cube base to screen out the parasitic frequencies.

The test results for the $\mathcal{X}$- and $\mathcal{Y}$-axes of the triangular Orchid W500P3 are shown in Fig. 7(a). The difference of the in-plane frequencies is 15.625 Hz, with a frequency mean value of 240.625 Hz and a deviation of 6.49%. Hence, the Orchid structure is proved to be isotropic in terms of in-plane frequencies. The small peak at around 900 Hz, apparent in Fig. 7(b), corresponds to the cube base frequency; it can therefore be dismissed.

The setup of the out-of-plane vibration is shown in Fig. 6(c), where a reference accelerometer was added for comparison with the measurement from the laser sensor. The out-of-plane frequency was not observed from the vibration test, as shown in Fig. 8, even upon exciting the samples at up to 5000 Hz. The magnification inside Fig. 8 shows the velocity response without any obvious resonance from 500 Hz to 5000 Hz. The disappearance of resonance peak,

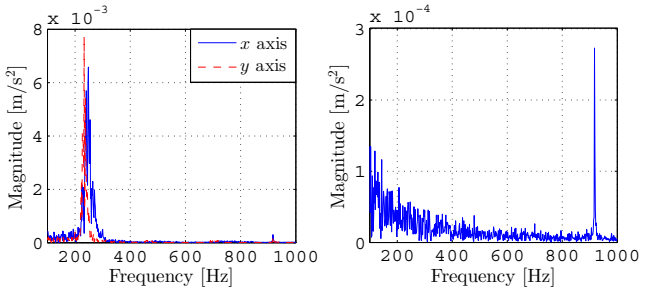


(a) (b)

Fig. 7. Vibration test of W500P3 for validation of in-plane isotropy: (a) in-plane frequencies; (b) base frequency

it is surmised, is caused by the significant squeezed-film air damping, where the air was trapped in the cavity between the large proof-mass area and the handle layer. This out-of-plane damping effect is beneficial to the frequency ratio, and hence, to the signal-to-noise ratio for the biaxial sensitivity.

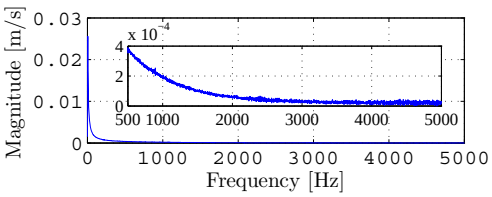


Fig. 8. Vibration test of W500P3 for out-of-plane stiffness

## 4 Conclusions

The novel design of the biaxial Orchid architecture exhibits high frequency ratios and isotropic stiffness. Under an aspect ratio of 16.7, the frequency ratio of the W500P3 is 6.36 with a fundamental frequency of 546 Hz in the sensitive plane. Under the simulated acceleration range of 10 $g$ per axis, the maximum stress with Lamé-curve fillets is 9.32 MPa. The vibration tests validate the elastically isotropic in-plane structure of the Orchid architecture for the triangular structure with an odd number of ΠΠ-hinges. The damping of the out-of-plane motion further increases the resistance in the insensitive directions, and hence, benefits the biaxial applications of the Orchid architecture.


## Acknowledgements

We would like to acknowledge CMC Microsystems for the provision of services that facilitated this research work. Professor Marco Amabili's Laboratory of Vibrations and Hydrodynamics is acknowledged for the provision of the vibration test. NSERC's support through a Discovery Grant is dutifully acknowledged. FRQNT's support through the New University Researchers Start-up Program is gratefully acknowledged. The MEDA scholarship from McGill University supported the first author at her PhD studies on biaxial accelerometers. The second author acknowledges the support provided by a James McGill Professorship.


## References


[1] Zou, T., and Angeles, J., 2014. "Isotropic accelerometer strapdowns and related algorithms for rigid-body pose and twist estimation". *Journal of Applied Mechanics,* **81**(11).

[2] Lee, J. S., and Lee, S. S., 2008. "An isotropic suspension system for a biaxial accelerometer using electroplated thick metal with a HAR SU-8 mold". *Journal of Micromechanics and Microengineering,* **18**(2).

[3] Herrera-May, A. L., and Bandala-Sanchez, M., 2013. "Design and modeling of a single-mass biaxial capacitive accelerometer based on the SUMMiT V process". *Microsystem Technologies,* **19**(12), pp. 1997–2009.

[4] Comi, C., Corigliano, A., Langfelder, G., and Tocchio, A., 2013. "Compact biaxial micromachined resonant accelerometer". *Journal of Micromechanics and Microengineering,* **23**(10).

[5] Zhao, H., Dai, B., and Liu, X., 2015. "A new silicon biaxial decoupled resonant micro-accelerometer". *Microsystem Technologies,* **21**(1), pp. 109–115.

[6] Zhao, J., Ju, B., and Xie, J., 2016. "A high-sensitivity biaxial resonant accelerometer with two-stage microleverage mechanisms". *Journal of Micromechanics and Microengineering,* **26**(1).

[7] Cardou, P., 2007. "Design of multiaxial accelerometers with simplicial architectures for rigid-body pose-and-twist estimation". PhD thesis, Department of Mechanical Engineering, McGill University, Montreal.

[8] Zou, T., 2013. "Design of biaxial accelerometers for rigid-body pose-and-twist estimation". PhD thesis, Department of Mechanical Engineering, McGill University, Montreal.

[9] Wohlhart, K., 1992. "Displacement analysis of the general spatial parallelogram manipulator". Proc. 3rd International Workshop on Advances in Robot Kinematics, pp. 104–111.

[10] Shan, X., Zou, T., Forbes, J., and Angeles, J., 2014. "Design of biaxial navigation-grade MEMS accelerometers". No. IMECE2014-37280, Proceedings of the ASME 2014 International Mechanical Engineering Congress & Exposition (IMECE2014).

[11] Han, F. T., You, P. C., Zhang, L., and Yan, X. J., 2015. "Experimental study of a low-$g$ micromachined electrostatically suspended accelerometer for space applications". *Microsystem Technologies,* **21**(1), pp. 29–39.

[12] Krishnamoorthy, U., Clews, P. J., Baker, M. S., and Tanner, D. M., 2008. "Challenges of designing and processing extreme low-$g$ micro electrical-mechanical system (MEMS) accelerometers". *Proceedings of the Society of Photo-optical Instrumentation Engineers (SPIE),* **6884**.

[13] Farin, G., and Hansford, D., 2005. *Practical Linear Algebra: A Geometry Toolbox*. A.K. Peters, Ltd., Wellesley, MA.